Computer Methods and Programs in Biomedicine 175 (2019) 1–7

Contents lists available at ScienceDirect

Computer Methods and Programs in Biomedicine

journal homepage: www.elsevier.com/locate/cmpb

Non-sedated functional imaging based on deep synchronization of PROPELLER MRI and NIRS

Liang Deng[a], Juntian Zhang[b], Jitao Chen[a], Zhihao Yu[a], Junrong Zheng[a,*]

[a] Beijing National Laboratory for Molecular Sciences, College of Chemistry and Molecular Engineering, Peking University, Beijing 100871, China
[b] Department of Pharmacology, Institute of Materia Medica, Chinese Academy of Medical Sciences, Beijing 100050, China

ARTICLE INFO

Article history:
Received 17 December 2018
Revised 1 March 2019
Accepted 20 March 2019

Keywords:
Non-sedated fMRI
PROPELLER
Near-infrared spectroscopy
BOLD signal
Multi-modality

ABSTRACT

Background and Objective: Periodically rotated overlapping parallel lines with enhanced reconstruction-echo planar imaging (PROPELLER-EPI) is a promising technique for non-sedated functional imaging due to its unique advantage of motion correction. However, its multiple-blades sampling blood-oxygen-level dependent (BOLD) signal leads to low sampling rate and aliasing of higher frequency physiological signal components such as the cardiac pulsation.

Methods: In this study, we use near infrared spectroscopy (NIRS) synchronized with pulse sequences of PROPELLER-EPI, utilizing the fact that the optical sensing speed is inherently high. NIRS measures changes of oxyhemoglobin and deoxyhemoglobin to identify the transient states of on-BOLD and off-BOLD, and then labels each blade by temporal co-registration. The labeled blades from multiple epochs of a functional experiment are then used for the *k*-space data combination and subsequent image reconstruction. An eigenfunction model is proposed for temporal co-registration and to quantify the temporal resolution of the hemodynamic response.

Result: The experiment of NIRS labeled PROPELLER-EPI was carried out with the optical sampling rate of 10 Hz and the magnetic pulses repetition time of 1000 ms, and the temporal resolution is 20 times better than that of the state-of-the-art sliding-window PROPELLER-EPI. We compared the functional imaging results against the conventional magnetic resonance echo planar imaging-measured activity and achieved an accuracy of 0.9.

Conclusions: Using the synchronization of NIRS, the proposed imaging scheme provides an effective way to implement PROPELLER-EPI, which features motion free, high SNR, and enhanced spatial-temporal resolution.

1. Introduction

Non-sedated functional imaging is of great importance for young children who require sedation or general anesthesia in conventional MRI (magnetic resonance imaging) studies [1,2]. Also, the high field small animal MRI is an efficient tool for experimental pathology and pharmacology in brain research [3–6], and non-sedated small animal imaging is an essential tool for longitudinal functional changes studies. Moreover, such movement-allowed imaging techniques can be used to scan a patient or animal concurrently performing several neural tasks. PROPELLER-EPI is a method that can suppress motion artifacts so that the imaging object can move freely during the time-consuming MRI scans [7–11]. Thus the risks of sedation or anesthesia can be avoided. The periodically rotated overlapping parallel lines with enhanced reconstruction-echo planar imaging (PROPELLER-EPI) is a multi-shot method to achieve the *k*-space time division coverage. It allows each blade to enable extended *k*-space sampling along the readout direction, to satisfy the temporal resolution of fMRI (functional MRI) activation, and to be imaged separately. Thus the motion correction in the image domain between successive blade shots is applicable. Among many PROPELLER approaches, the sliding-window reconstruction is a state-of-the-art approach that continuously reconstructs an image with each newly acquired blade, while dropping the first blade of an updated set. However, the temporal resolution level is still not enough to anti-aliasing of physiological interference. Also, the PROPELER-EPI imaging can suffer from the mis-alignments between blades and epochs of functional blood-oxygen-level dependent (BOLD) states, producing false BOLD signals.

Near-infrared spectroscopy (NIRS) measures the changes in brain hemodynamics and oxygenation during the neural activity with high temporal resolution [12–23]. It is known that the

* Corresponding author.
E-mail address: junrong@pku.edu.cn (J. Zheng).

https://doi.org/10.1016/j.cmpb.2019.03.016
0169-2607/

temporal resolution of fMRI is relatively low, while that of NIRS is generally high enough to sample most physiological processes without aliasing [22]. Therefore, concurrent NIRS and fMRI processing can be used to identify spatial and temporal effects of cardiac pulsation, breathing, and low frequency oscillations [20]. Multimodal analysis of MRI combined with NIRS has been introduced to correlate neural activity based on hemodynamics [17], for examples, to interpret the complex coupling among cerebral blood flow (CBF), cerebral blood volume (CBV) and cerebral metabolic rate of oxygen consumption ($CMRO_2$), and to examine neural activity patterns triggered by cognitive or perceptual tasks as well as resting state networks [22].

However, the fMRI/NIRS multimodal analysis encounters many difficulties in automatic mapping, image reconstruction and temporal alignment. NIRS is a cortical approach with low spatial resolution (~1 cm) and short depth of penetration (~2 cm) [20], limiting its effectiveness for the MRI mapping of the deep brain region. To address this issue, a support vector regression learning algorithm is developed to infer deep-brain activity using NIRS measurements of cortical activity [24]. Also, 3D reconstruction methods are developed to project channel-space on the surface of the head to voxel-space within the brain volume [25]. Nevertheless, most previous studies focus on investigating the temporal and spatial correlations between the MRI and NIRS signals [17,18,20,22]. In other words, MRI and NIRS data are processed independently (referred as "post synchronization" of MRI and NIRS). In this work, instead of comparing results from both MRI and NIRS measurements, NIRS signals are used in MRI data processing to correct imaging misalignments (referred as "deep synchronization" of both). In our approach, *k*-space data are acquired by a multi-shot PROPELLER-EPI technique with time division coverage. Each blade of the *k*-space data is labeled by NIRS output based on an eigenfunction model. Multiple labeled blades of one image are sampled during multiple activation and resting periods. The labeled blades are then combined and reconstructed. In this way, the multimodal imaging scheme of PROPELLER MRI deeply synchronized by NIRS is able to reconstruct the functional image with enhanced spatio/temporal resolutions, and without sedation.

2. Material and methods

2.1. Theory

2.1.1. Background on PROPELLER-EPI gradient function and temporal progress

Along the frequency encoding (readout) direction, the gradient function within each data acquisition time T_{acq} can be express as

$$\begin{cases} G_x = (-1)^{n-1} A \cos l\phi \\ G_y = (-1)^{n-1} A \sin l\phi \end{cases}, \tag{1}$$

where A is a constant to be determined, n is the number of frequency encodings, l is the number of blades, and $l\phi$ is the angle between the frequency encoding direction and k_x-axis (noting that blade rotates counterclockwise from the positive x-axis). Similarly, along the phase encoding direction the gradient function within each phase encoding time T_{pe} is

$$\begin{cases} G_x = -B \sin l\phi \\ G_y = B \cos l\phi \end{cases}, \tag{2}$$

where B is a constant to be determined. The *k*-space sampling trajectory in the presence of the gradient is showed in Fig. 1. Eq. (1) describes the sampling trajectory of blue lines, and Eq. (2) describes the sampling trajectory of red lines. These equations provide insight into the information of the temporal trace.

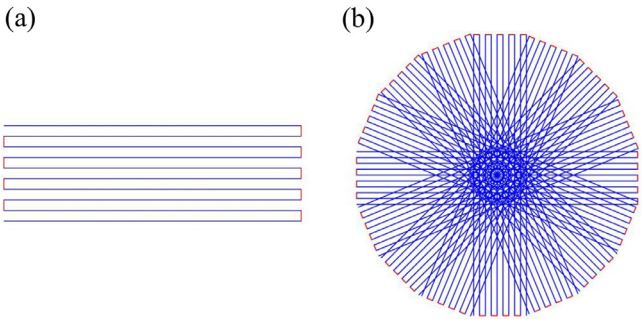

Fig. 1. PROPELLER-EPI acquisition scheme showing (a) one blade acquired using a single RF-excitation followed by fast gradient echo EPI readout and (b) 8 periodically rotated blades to fill the *k*-space.

The time node of the lth blade is lT_R, and the duration of the effective spatial-information-encoded echo signal acquisition of each blade is $nT_{acq}+(n-1)T_{pe}$. Other parameters of the pulse sequences are also known. Thus the full time course is determined. In this way, the temporal co-registration-based analysis can be realized and even the feedback control with NIRS data is applicable.

2.1.2. NIRS signal model

In this model, we use the variations of the deoxyhemoglobin concentration as the determinant of BOLD responses. In the wavelength range between 650 and 950 nm, the dominant absorbent chromophores are oxyhemoglobin and deoxyhemoglobin. The two wavelengths detection method expresses the variations in the local deoxyhemoglobin concentrations Δ[Hb] as

$$\Delta[\mathrm{Hb}] = \frac{\det\begin{bmatrix} \chi_{\mathrm{HbO}}(\lambda_1) & \Delta\mu(\lambda_1) \\ \chi_{\mathrm{HbO}}(\lambda_2) & \Delta\mu(\lambda_2) \end{bmatrix}}{\det\begin{bmatrix} \chi_{\mathrm{HbO}}(\lambda_1) & \chi_{\mathrm{Hb}}(\lambda_1) \\ \chi_{\mathrm{HbO}}(\lambda_2) & \chi_{\mathrm{Hb}}(\lambda_2) \end{bmatrix}}, \tag{3}$$

where $\mu(\lambda)$ is the absorption coefficient of λ, $\chi_{\mathrm{HbO}}(\lambda)$ and $\chi_{\mathrm{Hb}}(\lambda)$ denote the wavelength dependent extinction coefficients of the chromophores, and det is the determinant of the matrix. According to the modified Lambert-Beer law, the absorption coefficient at each wavelength is related to the optical density by the following formula:

$$\Delta\mu(\lambda) = -\frac{1}{L(\lambda)} \log\left(\frac{I(n,\lambda)}{I(n-1,\lambda)}\right), \tag{4}$$

where $I(n, \lambda)$ is the nth sample of the average intensity of detected light, and $L(\lambda)$ is the effective average pathlength of light through the tissue.

2.1.3. Proposed synchronization reconstruction scheme

The default PROPELLER reconstruction requires N blades for a full image, but the resulting temporal resolution would be unacceptable for fMRI. To overcome this problem, we label each blade with either transient state of the BOLD-NIRS signal: (1) on-BOLD or (2) off-BOLD. The on-BOLD state refers to the interval between the initial dip and the poststimulus over/undershoot, and the off-BOLD state refers to the transient of poststimulus over/undershoot and the resting state baseline. We present an eigenfunction model of the changes of the normalized deoxyhemoglobin concentration q as

$$q(t) = \begin{cases} q(0+)e^{-at}, 0 \le t < \tau \\ A(1 - e^{-b(t-\tau)}) + q(\tau)e^{-b(t-\tau)}, t \ge \tau \end{cases}, \tag{5}$$

where $q(0_+)$ is the concentration [Hb] at the initial dip, τ is the rising time of CBF response, A is a quantity correlated to the cerebral metabolic rate of oxygen ($CMRO_2$), and a, b are constants to be

determined. Similarly, the negative BOLD responses can be modeled as

$$q(t) = \begin{cases} A(1 - e^{-b^t}) + q(0_+)e^{-bt}, 0 \le t < \tau \\ q(\tau)e^{-a(t-\tau)}, t \ge \tau \end{cases}, \quad (6)$$

The acquired NIRS data can use the model as a regression function, and *a, b* and *A* can be determined by solving a least-squares problem. Then we define the baseline crossing interval T_{on} as on-BOLD state and others as off-bold state. This eigenfunction model highlights its versatility with respect to fMRI-NIRS co-registration.

After all blades are labeled, the temporal progress of BOLD signal is fully determined. Then, the spatial distribution of BOLD signal can be determined by the PROPELLER scheme. Both *N* blades labeled with on-BOLD and *N* blades labeled with off-BOLD are overlapped as *k*-space data, and the DFT (Discrete Fourier Transform) reconstruction is to be performed to obtain functional encoded images. Processing the non-Cartesian data acquired by each blade and gridding to Cartesian coordinate are essential to generate function $k(t)$ of the full *k*-space data. The continuous function $k(t)$ can be reconstructed optimally in the DFT framework by using the following interpolation formula:

$$k(t) = \sum_{n=0}^{N_s-1} k(n\Delta t) \frac{\sin[\frac{\pi}{T}(2N+1)(t-n\Delta t)]}{N_s \sin[\frac{\pi}{T}(t-n\Delta t)]}, \quad (7)$$

assuming that $N_s \ge 2N+1$ samples are taken from $k(t)$ in interval $\Delta t = T/N_s$. Finally, note that the density compensation of the combination of the blades is performed by using 2D Gaussian filter, and motion displacement parameters can be solved by mutual information method in image domain [26].

2.1.4. fMRI analysis

We are not using the SPM (Statistical Parametric Mapping) method in which the time-course is determined by convolving the hemodynamic response function [27], since the on-BOLD time-course is determined by NIRS with a high temporal resolution. To exploit the deep synchronization reconstruction for high temporal resolution fMRI, Pearson's correlation coefficient is calculated using a special strategy. The images reconstructed by on-BOLD blades are denoted $D_1 = \{X_i\}_{i=1}^L$, whereas the images reconstructed by off-BOLD blades are denoted $D_2 = \{Y_i\}_{i=1}^L$. The correlation coefficient r_{mn} of the voxel in position (m, n) used for fMRI analysis is given by

$$r_{mn} = \frac{\sum_{i=1}^{L} \left(X_i(m,n) - \bar{X}(m,n)\right)\left(Y_i(m,n) - \bar{Y}(m,n)\right)}{\sqrt{\sum_{i=1}^{L} \left(X_i(m,n) - \bar{X}(m,n)\right)^2} \sqrt{\sum_{i=1}^{L} \left(Y_i(m,n) - \bar{Y}(m,n)\right)^2}}, \quad (8)$$

Every voxel within the brain with a correlation coefficient *r* of 0.3 or lower is deemed activated by the functional task.

2.2. Data acquisition and experiments

2.2.1. NIRS data acquisition

NIRS measurements were taken with a home-built optical topography system. The imaging sequence used in this work and the communication interface software of MRI and NIRS were developed with python 3.6. Image reconstruction was performed off-line using MATLAB (R2015a, The MathWorks, Natick, MA). The system was designed to realize multiple sources of two wavelength time division multiplexing and multichannel signal sampling and communication, and the diagram of system is shown in Fig. 2. A field-programmable gate array (FPGA) was implemented as the microcontroller and data processor and the sampling rate was 10 Hz.

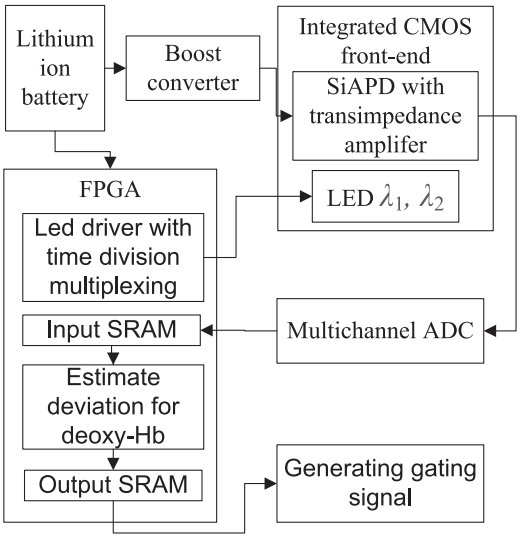

Fig. 2. Diagram of the optical system design and functional blocks of the FPGA-implementation.

The main technological characteristics of MRI-compatible materials are the magnetic susceptibility and the electrical conductivity. At first, the magnetic susceptibility difference between the material and tissue produces field inhomogeneities in the B_0 field, which leads to susceptibility artifacts. The illumination LEDs are coupled with the single-mode optical fibers, and the photodiodes are coupled with the multimodal optical fibers. A natural rubber pad is used to support these transmission optical fiber bundles. The magnetic susceptibilities of optical fiber material and natural rubber are within l ppm of biological tissue susceptibility. Secondly, the electrical conductivities of optic fiber material and natural rubber are negligible, so no eddy current issue is concerned.

2.2.2. MRI experiments

MRI data were acquired in vivo on a mouse using a 7T high field small animal MRI scanner (Agilent Technologies). The mouse was placed in a specially designed holder to immobilize the head, and a circular surface coil was employed as the RF transmitter/receiver. No anaesthesia was applied. fMRI data were acquired using GE-EPI (FOV = 35×35 mm^2, acquisition matrix of 256×50 per blade, 12 coronal slices each 0.5 mm thick, slice gap 0.1 mm, $T_R = 1000$ ms, $T_E = 36$ ms, bandwidth of 170 kHz). With the development of high-order gradient shim techniques and high magnetic field strength, the high anatomical contrast functional images were obtained at long TE [5]. All experiments were conducted in compliance with the regulations of Institute of Materia Medica, Chinese Academy of Medical Sciences.

2.2.3. Experimental protocol

The visual stimulus board is a rubber pad plugged with a set of optic fiber cables which transmit the lights of blue and green LEDs. The LEDs stimuli arrangement is displayed in Fig. 3. The LEDs are controlled by an Arduino microcontroller. Each LED is turned on for 100 ms, and the whole pattern period is 1.8 s. The round pad is suitable for the long, narrow scanner bores. Activation (stimulus-on) and resting (stimulus-off) periods of 18 s and 18 s, respectively, repeated for 20 times. These durations are long enough to allow for the exhaustion of functional response from one block to another. Consequently, for MRI a total of 720 blades for each slice are acquired and for NIRS 7200 samplings are acquired. Finally, a conventional EPI functional imaging is performed as the control data.

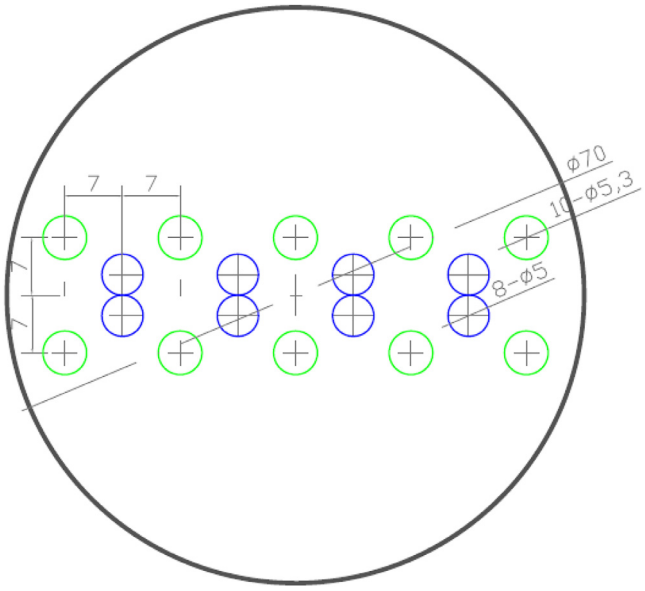

Fig. 3. Dimensions and arrangement of the visual stimulus board. Blue LEDs are plugged in the 8 holes along the central line on the pad, and the green LEDs were plugged in 10 peripheral holes.

3. Results

The results of NIRS signal detection and processing are displayed in Fig. 4. Concentration changes of oxy- and deoxy-hemoglobin are first calculated by the modified Beer-Lambert law, and then the Δ[HbO] and Δ[Hb] data are low-pass filtered with a Butterworth filter with order 6 and a cut-off frequency of 0.1 Hz.

Fig. 5 displays one set of representative images constructed by each blade labeled by NIRS. As can be seen, the images reconstructed by single blade show the Gibbs ringing artifacts along the direction of short axis of blades. However, this would not affect the image domain motion correction implementation because the high spatial resolution and high anatomical contrast. The combination of 8 labeled blades and its imaging result are displayed in Fig. 6. The ringing artifacts disappear and the resolution is apparently higher. Noted that the combined *k*-space data are filtered by the 2D Gaussian window with a standard deviation $\sigma=128$.

The BOLD responses to the visual stimulation are observed in the dorsal lateral geniculate nucleus (LGd) of the thalamus and the activation maps are displayed in Fig. 7. The activation voxels are identified by the proposed functional analysis in which the dataset of on-BOLD images are compared against the dataset of off-BOLD images using the Pearson's correlation.

Finally, the temporal resolution is determined by the NIRS modality which is equal to the sensing speed of the optical set-up. More exactly, the optical sensing speed depends on the sampling periods T_s $(1/f_s)$ or the duration of the light pulse T_p, and the improvement factor of temporal resolution of NIRS labeled PROPELLER-EPI is

$$\frac{2\mathrm{TR}}{\min(T_s,\ T_p)}, \tag{9}$$

The temporal resolution in our experiment protocol, for instance, improves by a factor of 20 than that of sliding-window PROPELLER-EPI. The mean correlation calculated by the functional activation maps between the results and the control data is higher than 0.9.

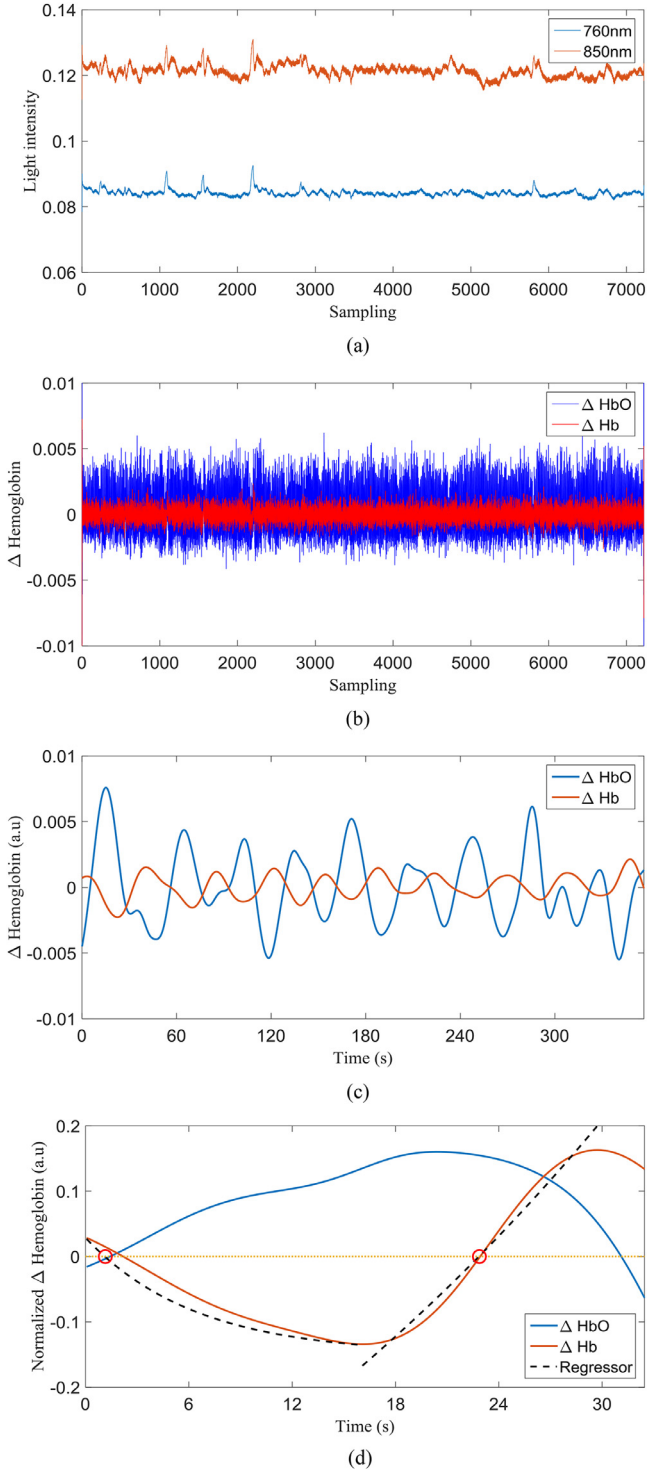

Fig. 4. A temporal trace of BOLD-NIRS response recorded in one functional experiment. Raw data at two wavelengths are shown in (a), and the Δ[HbO] and Δ[Hb] calculated by the modified Beer-Lambert law are shown in (b). A typical segment of the Δ[HbO] and Δ[Hb] signals after low-pass filtering is shown in (c), and an activation epoch is extracted as shown in (d). The interval between two zero crossings intercepted by regressors (red spots) is defined as the on-BOLD state.

4. Discussion

4.1. The balloon model and the eigenfunction model of the hemodynamic response

A popular biophysical model describing different transient states of the hemodynamic response is the balloon model [28]. The

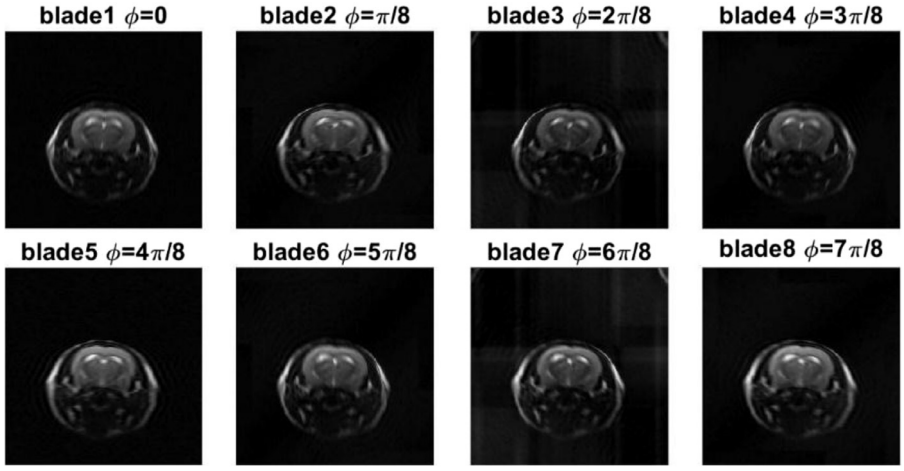

Fig. 5. Images constructed by each blade labeled by NIRS.

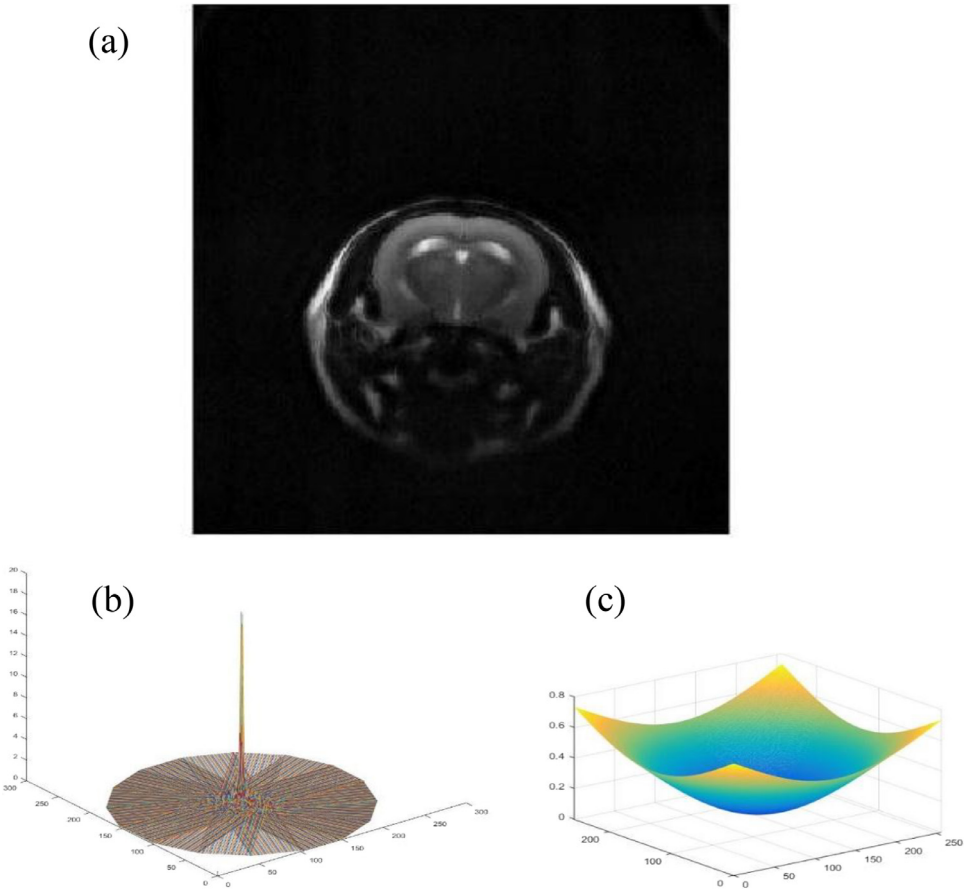

Fig. 6. Illustration of k-space data processing and reconstruction. (a) Imaging result of one slice using NIRS labeled PROPELLER-EPI scheme with $N=8$ blades. (b) The combined k-space data of $N=8$ blades filtered by the 2D Gaussian window. (c) The 2D gaussian window used to compensate the oversampled k-space center ($\sigma=128$).

model assumes that the venous balloon constitutes the only origin of the change in CBV and is expanded by a difference in normalized arterial inflow $f_{\text{in}}(t)$ and normalized venous outflow $f_{\text{out}}(t)$. The changes of the normalized deoxyhemoglobin concentration q can be modeled as:

$$dq/dt = 1/\tau_0\left[f_{\text{in}}(t)E(t) - f_{\text{out}}(v,t)\frac{q(t)}{v(t)}\right], \tag{10}$$

where v is the blood volume, τ is the viscoelastic time constant, $E(t)$ the cerebral metabolic rate of oxygen.

The balloon model is not the only physiological mechanism of the BOLD response. For instance, the diffusion movement of molecules can take place from a region of high concentration to a region of low concentration [29]. The diffusion model can be written as

$$\frac{\partial n(\boldsymbol{r},t)}{\partial t} = n(t)E(t) + D\nabla^2 n(\boldsymbol{r},t), \tag{11}$$

where n is the concentration of the diffusing molecules, D is the diffusion coefficient, and $\boldsymbol{r}$ is the position. The diffusing molecules can be the oxyhemoglobin, deoxyhemoglobin or total hemoglobin.

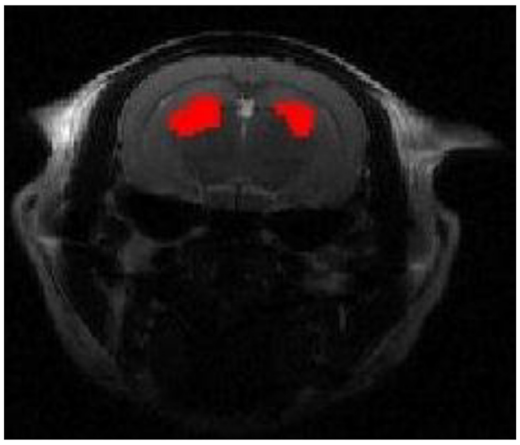

Fig. 7. BOLD responses to the visual stimulation in the coronal slices for observing LGd. The activated voxels calculated by the proposed method based on Pearson's correlation overlaid on one slice.

In mathematics, both the balloon model and the diffusion model is a class of differential operators on the space C^{∞} of infinitely differentiable functions of an argument t, and the exponential function is the eigenfunction of this linear operator. Therefore, we propose the eigenfunction model described in Eqs. (5) and (6), which is the solution for the purpose of the temporal co-registration and quantification analysis.

4.2. Theoretical analysis of SNR improvement of the NIRS-labeled PROPELLER-EPI

In our scheme the imaging blades may come from different epochs, so the variance of the noise from different blades could be time-varying. The linear combination of N blades reconstruction is related to the true image's k-space data by

$$\sum_{n=1}^{N} c_n S_n = \sum_{n=1}^{N} c_n S_{\text{true}} + \sum_{n=1}^{N} c_n \xi_n, \tag{12}$$

where $\boldsymbol{\xi}$ is the noise in the k-space domain, and $\boldsymbol{c}$ is a vector containing the weighting coefficients. The SNR formula can be derived as

$$\text{SNR}|_{\text{pixel}} = \frac{\sum_{n=1}^{N} c_n S_{\text{true}}}{\sqrt{\boldsymbol{c}^T \boldsymbol{\Sigma} \boldsymbol{c}}}, \tag{13}$$

where $\boldsymbol{\Sigma}$ is the matrix containing variance of each blade and has the form

$$\boldsymbol{\Sigma} = \begin{bmatrix} \sigma_{\xi_1}^2 & & & \\ & \sigma_{\xi_2}^2 & & \\ & & \ddots & \\ & & & \sigma_{\xi_n}^2 \end{bmatrix}. \tag{14}$$

The default choice of $\boldsymbol{c}$ is that all elements are equal to 1. Furthermore, assuming that $\xi_1,\ldots, \xi_n$ are zero-mean, independently and identically distributed random variables, the SNR in the central circle of k-space is improved by a factor of $\sqrt{N}$. In other words, a central circle in the k-space with diameter D is resampled for every blade, where D is the phase encoding width of each blade. At higher spatial frequencies, the overlap decreases, and the peripheral k-space values are only covered by one or two blades, as shown in Fig. 1(b) and Fig. 6(b).

The improvement in spatial localization of BOLD signal requires data with high spatial frequencies, but the SNR decreases at high spatial frequencies due to the signal strength decreases. To suppress the SNR decrease associated with extended k-space sampling, image reconstruction can be performed by solving a regularized least-squares optimization problem of the form

$$\hat{\boldsymbol{\rho}} = \arg\min_{\rho} \|\boldsymbol{S} - \mathcal{F}\{\boldsymbol{\rho}\boldsymbol{\Phi}\}\|_2^2 + \lambda \Psi(\rho, \boldsymbol{\Phi}), \tag{15}$$

where $\boldsymbol{\rho}$ is the spatial coefficients in image domain, $\boldsymbol{\Phi}$ is a set of voxel basis functions, f represents the Fourier transform operator, the $||\cdot||_2^2$ term measures the data consistency, and $\Psi(\cdot)$ is a regularization function with regularization parameter λ. There are many choices for $\Psi(\cdot)$ to incorporate prior information, such as quadratic and sparsity-promoting penalties [30–34].

4.3. Option of real-time gating

In this work, NIRS and fMRI experimental data are concurrently acquired. For future work, the real-time gating with NIRS feedback is conceivable. The NIRS system can generate a gating signal that trigs the pulse-sequence emitting system of MRI so that every blade contains only the on-state signal. In principle, both approaches would yield the same result. As briefly discussed above, the current method is based on a couple of assumptions: The cortical activity monitored by NIRS is assumed to be connected with the deep-brain activities, and the MRI is assumed to fulfill the task of functional imaging of arbitrary slices. For instance, defined in the Allen Mouse Brain Atlas in visual processing [6,35], the dorsal lateral geniculate nucleus (LGd) at deep brain (thalamus) are functional connected with the primary visual area of the cortex (VISp).

4.4. Future perspectives

The synchronization of MRI and NIRS in this study highlighted the image acquisition with emphasis on the precision of the spatial brain mapping and the temporal information of functional response. However, it is known that both modalities basically do not provide absolute concentrations measurements, but only relative ones. The absolute concentrations measurement can be important in some applications, such as cognitive load evaluation and disease evolution study [36,37]. The future multi-modality functional imaging with dedicated MRI sequences and models is doable for absolute measurement. Also, optimal wavelength choice in function of the stimulus [23] and the placing of the source/detectors for human objects are the important issues that should be addressed in the near future.

5. Conclusion

Instead of temporal co-registration using post-reconstruction results, a deep synchronization scheme of NIRS and PROPELLE-EPI is proposed and demonstrated to achieve high temporal resolution for non-sedative functional imaging. In this method, each blade of PROPELLER-EPI is labeled by optical sensing the temporal states of on-bold and off-bold before image reconstruction. The optical sensing can technically achieve even with a picosecond time resolution, and hence the temporal resolution is only determined by the data acquisition time for one blade, which can be faster than physiological "noises" such as cardiac pulsation. This approach provides an effective way to implement PROPELLER-EPI or other multi-shot sequences, which features motion free, high SNR, and enhanced spatial-temporal resolution.

Conflict of interest

There are no known conflicts of interest associated with this publication. The financial support of this work will not influence its outcome.

Acknowledgments

This work is supported by NSFC-21627805 and Raisecom Corporation (China).

References

[1] K. Rozovsky, E.C. Ventureyra, E. Miller, Fast-brain MRI in children is quick, without sedation, and radiation-free, but beware of limitations, J. Clin. Neurosci. 20 (3) (2013) 400–405.
[2] P.Y. Shen, A.E. Nidecker, E.A. Neufeld, et al., Non-sedated rapid volumetric proton density MRI predicts neonatal brachial plexus birth palsy functional outcome, J. Neuroimaging (2016).
[3] H. Benveniste, S. Blackband, MR microscopy and high resolution small animal MRI: applications in neuroscience research, Prog. Neurobiol. 67 (5) (2002) 393–420.
[4] G.B. Ko, H.S. Yoon, K.Y. Kim, et al., Simultaneous multi-parametric PET/MRI with silicon photomultiplier PET and ultra-high field MRI for small animal imaging, J. Nucl. Med. Offic. Pub. Soc. Nucl. Med. 57 (8) (2016) 1309.
[5] H. Lei, V. Mlynárik, N. Just, et al., Snapshot gradient-recalled echo-planar images of rat brains at long echo time at 9.4 T, Magn. Reson. Imaging 26 (7) (2008) 954–960.
[6] N. Arun, I.N. Christie, S.G. Solomon, et al., fMRI mapping of the visual system in the mouse brain with interleaved snapshot GE-EPI, Neuroimage 139 (2016) 337–345.
[7] J.G. Pipe, Motion correction with PROPELLER MRI: application to head motion and free-breathing cardiac imaging, Magn. Reson. Med. 42 (5) (1999) 963.
[8] A.A. Tamhane, K. Arfanakis, Motion correction in PROPELLER and Turboprop-MRI, Magnet. Reson. Med. Offic. J. Soc. Magnet. Reson. Med. 62 (1) (2009) 174.
[9] A.A. Tamhane, M.A. Anastasio, M. Gui, et al., Iterative image reconstruction for PROPELLER-MRI using the NonUniform Fast Fourier Transform, J. Magnet. Reson. Imag. JMRI 32 (1) (2010) 211–217.
[10] Y. Essa, H. Noam, U. Kâmil, High-field fMRI unveils orientation columns in humans, PNAS 105 (30) (2008) 10607.
[11] M. Krämer, T.H. Jochimsen, J.R. Reichenbach, Functional magnetic resonance imaging using PROPELLER-EPI, Magn. Reson. Med. 68 (1) (2012) 140–151.
[12] M.A. Franceschini, D.A. Boas, Noninvasive measurement of neuronal activity with near-infrared optical imaging, Neuroimage 21 (1) (2004) 372–386.
[13] B. Jalil, V. Hartwig, O. Salvetti, et al., Assessment of hand superficial oxygenation during ischemia/reperfusion in healthy subjects versus systemic sclerosis patients by 2D near infrared spectroscopic imaging, Comput. Methods Programs Biomed. (2017) S0169260717307794.
[14] A. Bozkurt, A. Rosen, H. Rosen, et al., A portable near infrared spectroscopy system for bedside monitoring of newborn brain, Biomed. Eng. Online 4 (1) (2005) 29.
[15] F. Normandin, M. Sawan, J. Faubert, A new integrated front-end for a noninvasive brain imaging system based on near-infrared spectroreflectometry, IEEE Trans. Circuits Syst. I Regul. Papers 52 (12) (2005) 2663–2671.
[16] F. Scholkmann, S. Kleiser, A.J. Metz, et al., A review on continuous wave functional near-infrared spectroscopy and imaging instrumentation and methodology, Neuroimage 85 (Pt 1) (2014) 6–27.
[17] A. Kleinschmidt, H. Obrig, M. Requardt, et al., Simultaneous recording of cerebral blood oxygenation changes during human brain activation by magnetic resonance imaging and near-infrared spectroscopy, J. Cereb. Blood Flow Metab. 16 (5) (1996) 817.
[18] J. Steinbrink, A. Villringer, F. Kempf, et al., Illuminating the BOLD signal: combined fMRI-fNIRS studies, Magn. Reson. Imaging 24 (4) (2006) 495–505.
[19] B.R. White, A.Z. Snyder, A.L. Cohen, et al., Resting-state functional connectivity in the human brain revealed with diffuse optical tomography, Neuroimage 47 (1) (2009) 148–156.
[20] Y. Tong, B.D. Frederick, Concurrent fNIRS and fMRI processing allows independent visualization of the propagation of pressure waves and bulk blood flow in the cerebral vasculature, Neuroimage 61 (4) (2012) 1419.
[21] E. Maggioni, E. Molteni, C. Zucca, et al., Investigation of negative BOLD responses in human brain through NIRS technique. A visual stimulation study, Neuroimage 108 (2015) 410–422.
[22] L. Duan, Y.J. Zhang, C.Z. Zhu, Quantitative comparison of resting-state functional connectivity derived from fNIRS and fMRI: a simultaneous recording study, Neuroimage 60 (4) (2012) 2008–2018.
[23] I. Schelkanova, V. Toronov, Optimal quantitation of the cerebral hemodynamic response in functional near-infrared spectroscopy, Opt. Express 18 (18) (2010) 19386–19395.
[24] N. Liu, X. Cui, D.M. Bryant, et al., Inferring deep-brain activity from cortical activity using functional near-infrared spectroscopy, Biomed. Opt. Exp. 6 (3) (2015) 1074–1089.
[25] S. Wijeakumar, T. Huppert, V.A. Magnotta, et al., Validating an image-based fNIRS approach with fMRI and a working memory task, Neuroimage 147 (2016) 204–218.
[26] A. Dame, E. Marchand, Second-order optimization of mutual information for real-time image registration, IEEE Trans. Image Process. 21 (9) (2012) 4190.
[27] K.J. Friston, P. Jezzard, R. Turner, Analysis of functional MRI time-series, Hum. Brain Mapp. 1 (2) (2010) 153–171.
[28] R.B. Buxton, K. Uludağ, D.J. Dubowitz, et al., Modeling the hemodynamic response to brain activation, Neuroimage 23 (23 Suppl 1) (2004) S220–S233.
[29] D. Liang, Wen-Hui, et al., In situ NMR diffusion coefficients assessment of lithium ion conductor using electrochemical priors and Arrhenius constraint——A computational study, Chin. Chem. Lett. 28 (2) (2017) 362–366.
[30] J.P. Haldar, D. Hernando, S.K. Song, Z.P. Liang, Anatomically constrained reconstruction from noisy data, Magn. Reson. Med. 59 (2008) 810–818.
[31] J. Kornak, K. Young, B.J. Soher, A.A. Maudsley, Bayesian k-space-time reconstruction of MR spectroscopic imaging for enhanced resolution, IEEE Trans. Med. Imag. 29 (2010) 1333–1350.
[32] Y. Zhang, R.E. Gabr, M. Schar, R.G. Weiss, P.A. Bottomley, Magnetic resonance spectroscopy with linear algebraic modeling (SLAM) for higher speed and sensitivity, J. Magn. Reson. 218 (2012) 66–76.
[33] I. Chatnuntawech, B. Bilgic, E. Adalsteinsson, Undersampled spectroscopic imaging with model-based reconstruction, in: Proceedings of the International Symposium on Magnetic Resonance in Medicine, Salt Lake City, Utah, USA, 2013, p. 3960.
[34] J. Kasten, F. Lazeyras, D. Van De Ville, Data-driven MRSI spectral localization via low-rank component analysis, IEEE Trans. Med. Imag. 32 (2013) 1853–1863.
[35] E.S. Lein, M.J. Hawrylycz, N. Ao, M. Ayres, A. Bensinger, A. Bernard, A.F. Boe, M.S. Boguski, K.S. Brockway, E.J. Byrnes, L. Chen, L. Chen, T.-M. Chen, M. Chi Chin, J. Chong, B.E. Crook, A. Czaplinska, C.N. Dang, S. Datta, N.R. Dee, A.L. Desaki, T. Desta, E. Diep, T.A. Dolbeare, M.J. Donelan, H.-W. Dong, J.G. Dougherty, B.J. Duncan, A.J. Ebbert, G. Eichele, L.K. Estin, C. Faber, B.A. Facer, R. Fields, S.R. Fischer, T.P. Fliss, C. Frensley, S.N. Gates, K.J. Glattfelder, K.R. Halverson, M.R. Hart, J.G. Hohmann, M.P. Howell, D.P. Jeung, R.A. Johnson, P.T. Karr, R. Kawal, J.M. Kidney, R.H. Knapik, C.L. Kuan, J.H. Lake, A.R. Laramee, K.D. Larsen, C. Lau, T.A. Lemon, A.J. Liang, Y. Liu, L.T. Luong, J. Michaels, J.J. Morgan, R.J. Morgan, M.T. Mortrud, N.F. Mosqueda, L.L. Ng, R. Ng, G.J. Orta, C.C. Overly, T.H. Pak, S.E. Parry, S.D. Pathak, O.C. Pearson, R.B. Puchalski, Z.L. Riley, H.R. Rockett, S.A. Rowland, J.J. Royall, M.J. Ruiz, N.R. Sarno, K. Schaffnit, N.V. Shapovalova, T. Sivisay, C.R. Slaughterbeck, S.C. Smith, K.A. Smith, B.I. Smith, A.J. Sodt, N.N. Stewart, K.-R. Stumpf, S.M. Sunkin, M. Sutram, A. Tam, C.D. Teemer, C. Thaller, C.L. Thompson, L.R. Varnam, A. Visel, R.M. Whitlock, P.E. Wohnoutka, C.K. Wolkey, V.Y. Wong, M. Wood, M.B. Yaylaoglu, R.C. Young, B.L. Youngstrom, X. Feng Yuan, B. Zhang, T.A. Zwingman, A.R. Jones, Genome-wide atlas of gene expression in the adult mouse brain, Nature 445 (2007) 168–176.
[36] S. Aydöre, M.K. Mihçak, K. Ciftçi, et al., On temporal connectivity of PFC via Gauss–Markov modeling of fNIRS signals, IEEE Trans. Biomed. Eng. 57 (3) (2009) 761–768.
[37] R.G. Wise, A.D. Harris, A.J. Stone, et al., Measurement of OEF and absolute $CMRO_2$: mRI-based methods using interleaved and combined hypercapnia and hyperoxia, Neuroimage 83 (Complete) (2013) 135–147.